CONDENSED MATTER PHYSICS

Anomalously field-susceptible spin clusters emerging in the electric-dipole liquid candidate κ-$(ET)_2Hg(SCN)_2Br$

Mizuki Urai[1]*, Kazuya Miyagawa[1], Yuta Watanabe[1], Elena I. Zhilyaeva[2], Svetlana A. Torunova[2], Rimma N. Lyubovskaya[2]†, Natalia Drichko[3,4], Kazushi Kanoda[1]*

Mutual interactions in many-body systems bring about various exotic phases, among which liquid-like states failing to order due to frustration are of keen interest. The organic system with an anisotropic triangular lattice of molecular dimers, κ-$(ET)_2Hg(SCN)_2Br$, has been suggested to host a dipole liquid arising from intradimer charge-imbalance instability, possibly offering an unprecedented stage for the spin degrees of freedom. Here, we show that an extraordinary unordered/unfrozen spin state having soft matter–like spatiotemporal characteristics emerges in this system. ^{1}H nuclear magnetic resonance (NMR) spectra and magnetization measurements indicate that gigantic, staggered moments are nonlinearly and inhomogeneously induced by a magnetic field, whereas the moments vanish in the zero-field limit. The analysis of the NMR relaxation rate signifies that the moments fluctuate at a characteristic frequency slowing down to below megahertz at low temperatures. The inhomogeneity, local correlation, and slow dynamics indicative of middle-scale dynamical correlation length of several nanometers suggest novel frustration-driven spin clusterization.

INTRODUCTION

Strongly correlated electron systems harbor a rich variety of unconventional phenomena with the intertwining of interactions and their quantum nature (*1*). Among these phenomena is the quantum spin liquid (QSL), in which spins are highly correlated with one another but do not order due to strong zero-point fluctuations. The quest for QSLs has been a focus of profound interest in the physics of interacting many-body quantum systems (*2*–*5*). The layered organic conductors, κ-$(ET)_2X$, where ET denotes bis(ethylenedithio)tetrathiafulvalene and X is a monovalent anion, have been studied as model systems exhibiting the Mott metal-insulator transition and include QSL candidates (*6*, *7*). A key ingredient for understanding the electronic states in κ-$(ET)_2X$ is the strongly dimerized ET molecules (*8*); the ET dimers are arranged to form anisotropic triangular lattices (Fig. 1). Given that ET dimers are regarded as supermolecules occupying lattice sites, the complicated crystal structure is modeled with an anisotropic triangular lattice hosting one hole with a spin-1/2 at each lattice site. This simplification provides a basis for understanding magnetism in the Mott insulating state of κ-$(ET)_2X$, including antiferromagnets κ-$(ET)_2Cu[N(CN)_2]Cl$ (*9*–*12*), deuterated κ-$(ET)_2Cu[N(CN)_2]Br$ (*13*, *14*), and the possible QSLs κ-$(ET)_2Cu_2(CN)_3$ (*15*) and κ-$(ET)_2Ag_2(CN)_3$ (*16*) (hereafter abbreviated as κ-Cu-Cl, κ-Cu-Br, κ-Cu-CN, and κ-Ag-CN, respectively). This simple model of molecular lattice neglects the internal degrees of freedom within ET dimers; however, recent theoretical calculations have suggested that the intradimer electronic degrees of freedom can play a vital role in the emergence of exotic states for the "dimer Mott insulators" (*17*, *18*). For instance, the relaxer-type dielectric anomaly observed for κ-Cu-CN (*19*) is argued to be a manifestation of the intradimer charge imbalance in the QSL state under debate (*19*–*22*). More recently, κ-$(ET)_2Hg(SCN)_2Br$ (κ-Hg-Br) (Fig. 1, A and B) has been suggested to host a quantum dipole liquid in which electric dipoles presumably created by intradimer charge imbalance remain fluctuating down to low temperatures (*23*). This system undergoes a first-order metal-insulator transition at T_{MI} ~ 90 K (*24*), and there is no clear evidence of charge order below T_{MI} in the optical and dielectric measurements (*23*, *24*); this is in contrast to an isostructural sister compound κ-$(ET)_2Hg(SCN)_2Cl$ (κ-Hg-Cl), which undergoes a charge-ordering metal-insulator transition at T_{MI} ~ 30 K (*25*, *26*). Since the two systems have quite similar transfer integrals (*27*), κ-Hg-Br is possibly at the phase border between the Mott insulator and the charge-ordered insulator. As shown by first-principles band structure calculations (*26*, *27*), the ET dimerization in κ-Hg-Br is so weak among κ-$(ET)_2X$ systems that a gap between the bonding and antibonding bands of the ET dimers vanishes or is only marginally open (Fig. 1D), leading to a band profile having both quarter-filled and half-filled natures; the former favors a charge-ordered insulator, whereas the latter favors a Mott insulator. This feature is also reproduced by the extended Hückel tight-binding band calculations (Fig. 1E). The spin state in such a marginal situation can be nontrivial because the spin-exchange interactions are affected by the charge fluctuations; the time scale of charge fluctuations in κ-Hg-Br obtained by motional narrowing analysis of the Raman spectra is ~1 THz (*23*), which is on the same order of magnitude as the typical spin exchange frequency in κ-type ET compounds, on the order of 10^2 K (*10*, *11*, *14*, *15*). To date, the magnetization has been reported to show nonlinear soft ferromagnetic (FM)–like behavior (*28*) with no hysteresis (*29*). The magnetization, e.g., at a magnetic field of 1 T, was approximately one order of magnitude larger than that of the well-studied typical dimer Mott insulators κ-Cu-Cl (*10*, *11*) and κ-Cu-Br (*14*). More recently, a ^{13}C nuclear magnetic resonance (NMR) study of κ-Hg-Br suggested that the spin state is highly disordered as a consequence of inhomogeneous short-range charge order at low temperatures below T_{MI}

[1]Department of Applied Physics, University of Tokyo, Tokyo 113-8656, Japan. [2]Institute of Problems of Chemical Physics RAS, 142432 Chernogolovka, Russia. [3]The Institute for Quantum Matter and the Department of Physics and Astronomy, The Johns Hopkins University, Baltimore, MD 21218, USA. [4]The Institute for Solid State Physics, University of Tokyo, Kashiwa, Chiba 277-8581, Japan.
†Deceased.
*Corresponding author. Email: urai@mdf2.t.u-tokyo.ac.jp (M.U.); kanoda@ap.t.u-tokyo.ac.jp (K.K.)

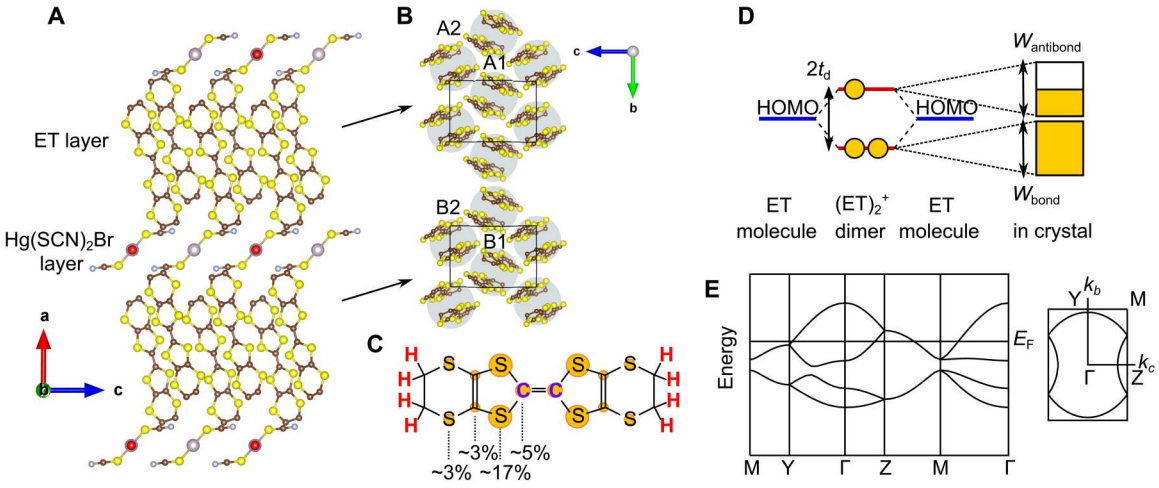

Fig. 1. Crystal and electronic structure of κ-Hg-Br. (**A**) Crystal structure (*61*). The conducting ET and blocking $Hg(SCN)_2Br$ layers alternately stack. There are two kinds of ET layers (A and B), the top view of which is shown in (**B**). Each pair of the ET molecules facing each other forms a dimer. The solid lines in (A) and (B) represent a unit cell. (A) and (B) were drawn using the visualizing software VESTA (*71*). (**C**) Structure of ET molecule. Densities of the highest-occupied molecular orbitals (HOMOs), the Mulliken populations, per atom are displayed. (**D**) Schematic electronic structure. In κ-$(ET)_2X$, two ET HOMOs in a dimer form bonding and antibonding orbitals through the intradimer transfer energy t_d, and each of them forms a conduction sub-band with the bandwidth, W_{bond} or $W_{antibond}$. In the case of κ-Hg-Br, the bandgap between the bonding and antibonding bands is narrow or vanishing, as seen in (E). (**E**) Band structure (left) and Fermi surface (right) of κ-Hg-Br based on the reported crystal structure (*61*). The range of vertical axis in the left is from −0.7 to 0.7 eV. The Mulliken populations, transfer integrals, and band dispersion were obtained by the extended Hückel method and tight-binding calculation, using the program package (*31*).

(*30*). The microscopic spin state that gives rise to such extraordinary magnetic properties has yet to be clarified.

The present work uses ^{1}H NMR spectroscopy with the magnetic field varied over a 20-fold range from 0.30 to 6.00 T, combined with spectral simulations, to clarify the microscopic local moment configuration and its field and temperature dependence in κ-Hg-Br. There are a total of eight protons in the ET molecule, each of which belongs to the ethylene groups at the edges of ET, as displayed in Fig. 1C. At the ^{1}H sites, because of the poor densities of the highest-occupied molecular orbitals (HOMOs), the hyperfine coupling is much smaller than that at the central double-bonded carbon sites (denoted by "C" and colored purple in Fig. 1C), which were ^{13}C-enriched in the previous ^{13}C NMR study by Le *et al.* (*30*). On the other hand, ^{1}H NMR is superior to ^{13}C NMR in capturing the widespread spectra at high fields, since it is difficult to acquire the entire spectrum with ^{13}C NMR due to the large hyperfine coupling. Here, we report that an anomalously field-susceptible unordered/unfrozen spin state with highly correlated characteristics emerges in κ-Hg-Br. We confirmed that the fundamental features of ^{1}H NMR and magnetization presented here were reproduced in different crystals (see the Supplementary Materials).

RESULTS

^{1}H NMR spectra

Figure 2 (A to D) displays the ^{1}H NMR spectra of κ-Hg-Br acquired in magnetic fields of 0.30, 1.00, 3.66, and 6.00 T, respectively. At high temperatures above T_{MI} (~90 K), the spectrum broadens slightly as the temperature decreases but is rather temperature insensitive. Upon further cooling, the spectrum is symmetrically broadened in every field. A structureless and broadened line shape indicates an inhomogeneous distribution of the local fields in contrast to discrete spectral lines, as observed in the commensurate antiferromagnet, κ-Cu-Cl (*9*). Incommensurate magnetic order is ruled out, as it would give a distinctive spectral shape with wings on the edges. This low-temperature spectral broadening reproduces the temperature dependence of the ^{13}C NMR spectra (*30*), thereby confirming that the line broadening is an intrinsic phenomenon. At a temperature of 2 K, and a field of 0.30 T, the spectra are extended to ±200 kHz, which exceeds the spectral width, ±100 kHz, observed for κ-Cu-Cl with an AF moment of 0.45 μ_B per dimer (μ_B is the Bohr magneton) (*7*), suggesting that the maximum moment amounts to ~1 μ_B per dimer or larger, as discussed in detail later. The spectral broadening is characterized by the square root of the second moment of the spectrum, $\langle\Delta f^2\rangle^{1/2}$, which is a measure of averaged local fields projected along the field direction, as shown in Fig. 2E. It is clear that $\langle\Delta f^2\rangle^{1/2}$ increases prominently below a certain temperature depending on the magnetic field. $\langle\Delta f^2\rangle^{1/2}$ does not show such an abrupt increase at T_{MI} on cooling, as in ^{13}C NMR (*30*), because the small Fermi contact interactions for proton nuclei caused by low electron spin densities (see Fig. 1C) give rise to no appreciable change in ^{1}H NMR spectral shift at the metal-insulator transition.

To gain insight into the configuration of the local moments indicated by the spectral broadening, we simulated the ^{1}H NMR spectra for several conceivable cases of collinear spin configurations. Because the proton nuclei in ET have negligibly small Fermi contact interactions, the local fields at the ^{1}H sites are evaluated by adding up the dipolar fields from electronic moments on the constituent atomic sites. Using the Mulliken populations for the spin-density distribution in ET (*31*) and the crystal structure for the ET arrangement (*25*), we summed up the dipolar contributions from the atomic sites within a sphere of radius ~ 100 Å (see Materials and Methods for details). Figure 3A shows the spectra calculated with a moment of 1 μ_B on an ET dimer for intradimer spin-density profiles (Fig. 3B) and interdimer spin configurations

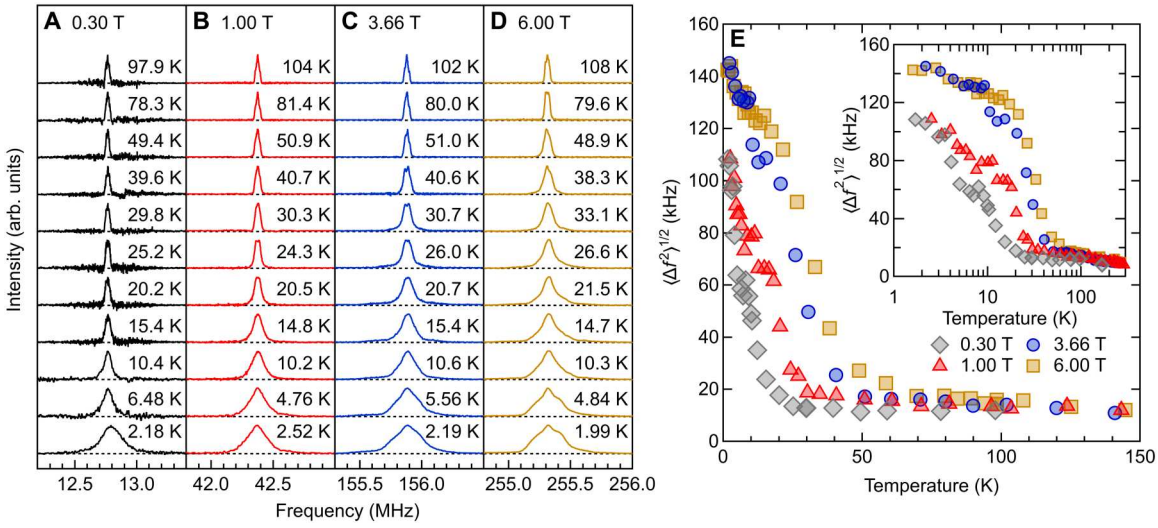

Fig. 2. ^{1}H NMR spectral profiles. (**A** to **D**) ^{1}H NMR spectra measured in magnetic fields of (A) 0.30, (B) 1.00, (C) 3.66, and (D) 6.00 T. (**E**) Temperature dependence of the square root of second moment of ^{1}H NMR spectra, $\langle \Delta f^2 \rangle^{1/2}$. The inset shows the same data in the entire temperature range up to 300 K.

(Fig. 3C) where the FM spins are parallel to the applied field and antiferromagnetic (AFM) spins are directed parallel (AFM I) or perpendicular (AFM II) to the field (normal to the layers); for AFM II, the moment direction is varied in the perpendicular plane. The FM configuration gives a spectrum shifted to one side, contradicting the observation; thus, this case is ruled out. Both AFM I and II have interlayer FM and AFM cases. Although the spectra for AFM II with the moments on the dimers aligned mutually parallel between the neighboring layers are slightly asymmetric owing to the glide symmetry of the crystal structure, all of the simulated spectra for AFM I and II are roughly symmetrical and able to explain the observation given an inhomogeneous distribution in the magnitude of the moment.

Staggered and uniform magnetizations

The second moment, $\langle \Delta f^2 \rangle$, gives estimates of the averaged magnitude of inhomogeneous staggered moments. $\langle \Delta f^2 \rangle$ is a sum of the temperature (T)– and field (H)–insensitive nuclear dipolar contributions, $\langle \Delta f^2 \rangle_n$, and the electron moment contribution of interest, $\langle \Delta f^2 \rangle_m$. Above T_{MI}, the ^{1}H NMR spectra are solely determined by the nuclear dipolar interactions. A slight increase of $\langle \Delta f^2 \rangle$ from room temperature is ascribable to the slowing down of the vibrational motion of the ethylene groups in ET, as indicated by the ^{1}H nuclear spin-lattice relaxation (described later). For $\langle \Delta f^2 \rangle_n$, we took the $\langle \Delta f^2 \rangle$ value at 100 K ($>T_{MI}$); namely, $\langle \Delta f^2 \rangle_m = \langle \Delta f^2 \rangle - \langle \Delta f^2 \rangle_n = \langle \Delta f^2 \rangle - \langle \Delta f^2 \rangle_{100K}$. Then, the linewidth, $\langle \Delta f^2 \rangle_m^{1/2}$, should be proportional to the averaged local moment, m_{local}. The proportional coefficient, a, in $\langle \Delta f^2 \rangle_m^{1/2} = a m_{local}$ is determined from the simulated spectra for each spin configuration and $\langle \Delta f^2 \rangle_m$ depends linearly on m_{local} as shown in the Supplementary Materials. For AFM I, $a = 1.7 \times 10^2$ kHz/μ_B per ET dimer, and for AFM II, a varies in the range of 1.0×10^2 to 2.5×10^2 kHz/μ_B per ET dimer depending on the field direction (Fig. 3D). We also considered the case with the spin density imbalanced between two ET molecules in a dimer. The simulated spectra for a disproportionation ratio of 0.8:0.2, for example, take different shapes from the 0.5:0.5 case discussed above (Fig. 3A). Nevertheless, the two cases are nearly indistinguishable in $\langle \Delta f^2 \rangle_m^{1/2}$ and a (Fig. 3D). Thus, it is concluded that large moments emerge in the applied fields whether the spin density is imbalanced in a dimer or not. Below, we assume a to be in a range of 1.0×10^2 to 2.5×10^2 kHz/μ_B per ET dimer because the spin orientation angle is not known.

Figure 4A displays the temperature dependence of $\langle \Delta f^2 \rangle_m^{1/2} = (\langle \Delta f^2 \rangle - \langle \Delta f^2 \rangle_n)^{1/2}$ determined from the experimental spectra. $\langle \Delta f^2 \rangle_m^{1/2}$ prominently increases below 15, 25, 30 to 40, and 40 to 50 K in fields of 0.30, 1.00, 3.66, and 6.00 T, respectively. The temperature dependence of $\langle \Delta f^2 \rangle_m^{1/2}$ is similar to that of the magnetization, M (Fig. 4B), indicating that local moments develop along with uniform magnetization. Figure 4 (C and D) displays $\langle \Delta f^2 \rangle_m^{1/2}/\mu_0 H$ and M/H, where μ_0 denotes the magnetic constant, both of which are field dependent below ~30 K and follow the Curie-Weiss law with the apparent Weiss temperature of 20 to 25 K above 30 K (Fig. 4, E and F). The positive Weiss temperature derived from M/H (Fig. 4F) is consistent with the previous report (*29*). The right axes of Fig. 4A show the scales for m_{local}, obtained using $a = 1.0 \times 10^2$ and 2.5×10^2 kHz/μ_B per ET dimer, which give the maximum and minimum m_{local} values, respectively. m_{local} is 10 to 20 times larger than M in magnitude, indicating that the local moments are primarily staggered and weak FM components appear. The $\langle \Delta f^2 \rangle_m^{1/2}$ value of 108 kHz at 1.7 K in a field of 0.30 T corresponds to the moment $m_{local} = 0.4$ to 1.0 μ_B per ET dimer, which is comparable to or larger than the AFM moments of 0.45 μ_B per dimer in κ-Cu-Cl (*7*).

Figure 4G shows the field dependence of $\langle \Delta f^2 \rangle_m^{1/2}$. At 30 and 40 K, $\langle \Delta f^2 \rangle_m^{1/2}$ varies linearly with the applied field, whereas, at lower temperatures, the variations are nonlinear. Except at 2 and 3 K, both of the values of $\langle \Delta f^2 \rangle_m^{1/2}$ and M (Fig. 4H) appear to approach zero in the zero-field limit, which indicates that the magnetitic moments vanish in the zero-field limit, that is, the system is paramagnetic. In addition, a comparison of Fig. 4 (G and H) shows that the staggered moments grow more rapidly with increasing magnetic field than the weak FM moments. We note that at 2 and 3 K, exceptionally large local moments are induced by even a low field of 0.3 T, which is also visible as an additional increase in the T dependence

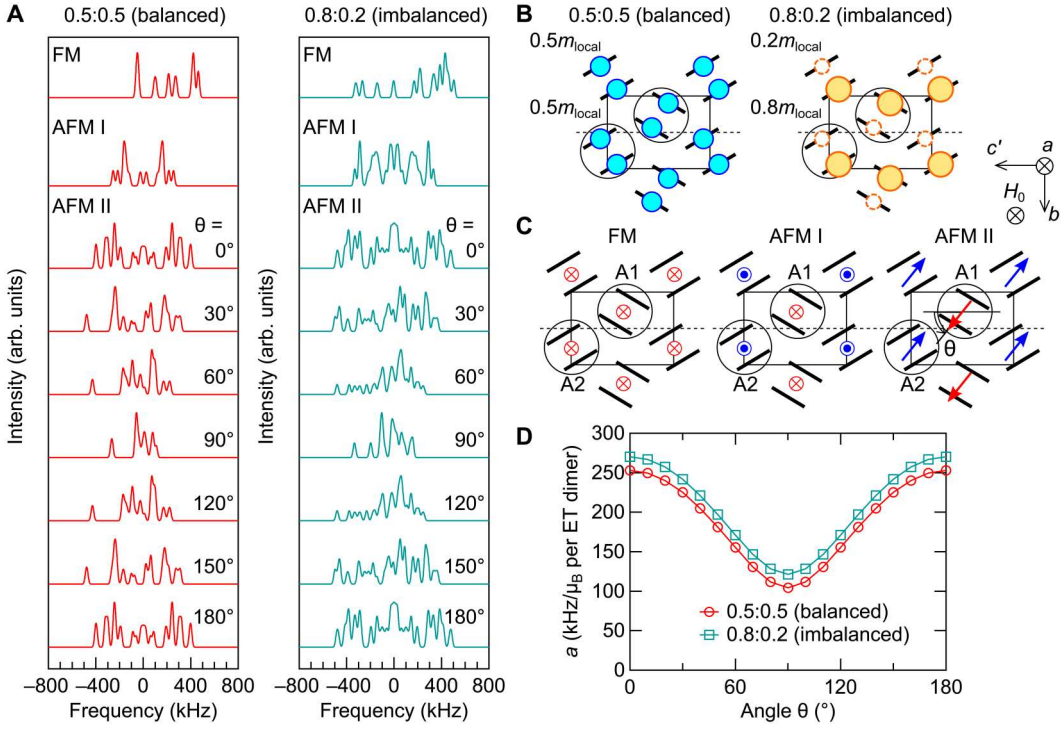

Fig. 3. Simulations of ^{1}H NMR spectra. (**A**) Calculated spectra with the moment of 1 μ_B on an ET dimer for the ferromagnetic (FM) configuration [left of (**C**)] and the antiferromagnetic (AFM) configurations with staggered moments directed parallel (AFM I) and perpendicular (AFM II) to the applied field (normal to the layers) [middle and right of (C)]. The left and right of (A) show the results for the cases with the intradimer spin-density disproportionation of 0.5:0.5 and 0.8:0.2, depicted in (**B**), respectively. For AFM II, the moment direction is varied in the perpendicular plane. (**D**) Angular dependence of the coefficient a, which relates the linewidth $\langle\Delta f^2\rangle_m^{1/2}$ and the size of the moment m_{local} in the form of $\langle\Delta f^2\rangle_m^{1/2} = am_{local}$ for AFM II. We assumed FM interlayer coupling for the simulations shown here. The values of $\langle\Delta f^2\rangle_m^{1/2}$ for the cases with AFM interlayer couplings are shown in the Supplementary Materials. The simulation of the spectrum in the case of $m_{local} = 0$ roughly reproduces the observed spectra above T_{MI} (see the Supplementary Materials).

of $\langle\Delta f^2\rangle_m^{1/2}$ below ~5 K (Fig. 4A). As M vanishes in the zero-field limit even at these temperatures (Fig. 4H), we consider that the staggered moments also vanish at a zero field but appear immediately upon applying low fields. We will discuss this low-temperature and low-field behavior later, taking into account the time scales of moment fluctuations and NMR observations.

ac susceptibility

Magnetization behavior in the low-field limit was examined by ac susceptibility (ac-χ) measurements. Figure 5A displays the real part of ac-χ (= m'/H_{ac}) with a frequency of 10 Hz and amplitudes, H_{ac}, of 1 and 4 Oe along with dc-χ (= M/H) at $\mu_0 H = 1$ T. The temperature dependence of m'/H_{ac} reproduces that of M/H well at high temperatures above 25 K, but it shows an upward deviation from M/H below that, consistent with the nonlinear magnetization that starts at approximately the same temperature (Fig. 4D). The low-temperature enhancement of m'/H_{ac} is more moderate than the Curie law and has the symptoms of saturation upon further cooling, as seen in the plot of the inverse of m'/H_{ac} (the inset of Fig. 5C), which indicates that all spins are interacting without free or orphan spins. m'/H_{ac} has neither amplitude dependence for H_{ac} = 1 and 4 Oe nor frequency dependence in the studied range of 1 to 100 Hz. Furthermore, the imaginary part of ac-χ, m''/H_{ac}, remains vanishingly small over the entire temperature range. All of these features demonstrate linear magnetization without jumps and hysteresis in the low-field limit, lending strong support to the absence of magnetic order or glassy spin freezing in κ-Hg-Br at least down to 1.8 K. Nevertheless, magnetic fields on the order of 1 T nonlinearly induce staggered moments as large as 0.4 to 1.0 μ_B on average per ET dimer even at temperatures as high as 20 K. This is a remarkable and unique feature of κ-Hg-Br.

^{1}H nuclear spin-lattice relaxation

Next, we present the nuclear spin-lattice relaxation rate, $1/T_1$, which probes the spectral density of spin fluctuations at the NMR frequency. T_1 was determined from the nuclear magnetization recovery over time, $M(t)$, after saturation, namely, $M(0) = 0$. $M(t)$ is a single exponential function of t at temperatures above 40 K; however, it gradually takes on a nonexponential character at lower temperatures (for the relaxation curves, see the Supplementary Materials). Thus, we determined T_1 by fitting the Kohlrausch function, $1 - M(t)/M(\infty) = \exp.[-(t/T_1)^\beta]$, to the data of $M(t)$. The exponent β characterizes the degree of inhomogeneity and approaches 1 in the homogeneous limit. In every measured magnetic field, the values of β stay in the range $\beta \gtrsim 0.9$ at high temperatures; however, they gradually decrease with temperature below ~30 K, as shown in Fig. 6A, indicating the evolution of inhomogeneities in spin dynamics at low temperatures. In magnetic fields of 1.00 to 6.00 T, β reaches a minimum value at approximately 7 to 10 K and increases upon further cooling, which seemingly suggests a recovery to

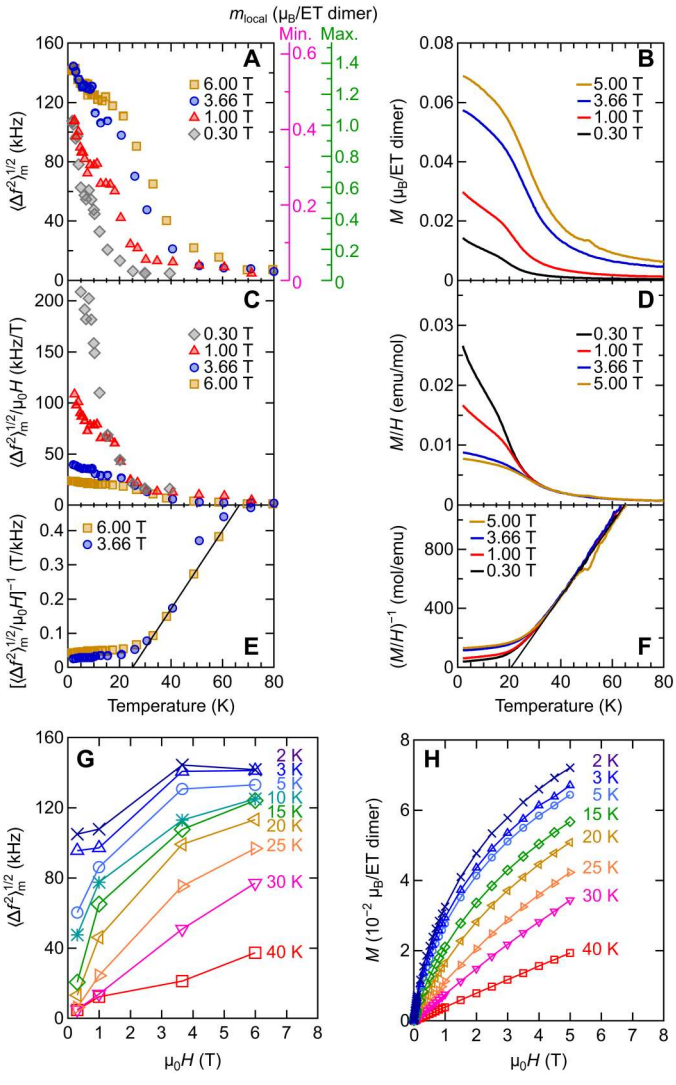

Fig. 4. Temperature dependence of local fields and dc magnetization. (**A** and **B**) Temperature dependence of (A) the square root of the electron moment contribution to second moment of ^{1}H NMR spectra, $\langle\Delta f^2\rangle_m^{1/2}$, and (B) dc magnetization, M. The right axes in (A) show the scales for the minimum (Min.) and maximum (Max.) values obtained for the size of the local moment, m_{local}, estimated in the present work (see the Supplementary Materials for details of the estimation). (**C** and **D**) Temperature dependence of (C) $\langle\Delta f^2\rangle_m^{1/2}/\mu_0 H$, (D) M/H, and their inverse [(**E**) and (**F**)]. (**G** and **H**) Field dependence of (G) the electron moment contribution to second moment of ^{1}H NMR spectra, $\langle\Delta f^2\rangle_m^{1/2}$, and (H) M at various temperatures.

homogeneous relaxation. However, this is presumably not the case but results from averaging of the inhomogeneous $1/T_1$ by spin-spin relaxation (T_2 process), which is particularly effective when T_1 is long. The absence of an upturn in β in a field of 0.30 T supports the idea that T_2 averaging is particularly effective in higher fields, where T_1 is an order of magnitude longer than in 0.30 T.

Figure 6B shows the temperature dependence of $1/T_1$ in magnetic fields of 0.30, 1.00, 3.66, and 6.00 T. A frequency-dependent peak structure arises at approximately 200 to 300 K due to the slowing down of the vibrational motion of ethylene groups located at the edges of an ET molecule (Fig. 1C), which is commonly observed for ET compounds (*9*, *32*–*34*). When cooled down across 85 to 89 K, $1/T_1$ shows an abrupt increase. This coincides with the jump and thermal hysteresis in M/H, which is concomitant with the metal-insulator transition, indicating that $1/T_1$ is determined by the electron moments below T_{MI}. Upon further cooling, $1/T_1$ gradually increases and forms a prominent peak at 7 to 9 K depending on the applied field. A similar peak in $1/T_1$ was observed by ^{13}C NMR (*30*), although the peak structure was broader and the peak temperature was lower than in ^{1}H NMR, partially because, in ^{13}C NMR, $1/T_1$ must be determined by the relaxation of only the fractional spectrum that was covered by the radio-frequency (rf) pulse. The $1/T_1$ values at low temperatures are strongly suppressed as the magnetic field is increased from 0.30 to 6.00 T. At first sight, the peak formation of $1/T_1$ is reminiscent of a magnetic transition; however, the observed features are very different from the indications of a magnetic transition, as follows. In the case of a magnetic transition, a peak in $1/T_1$ occurs at a temperature, T_c, at which spin moments start to emerge, as is observed for κ-Cu-Cl (*9*). This is because upon cooling from above T_c, the spin fluctuations slow to cause a critical increase in $1/T_1$ near T_c, and upon further cooling below T_c, where ordered moments develop, spin-wave excitations responsible for $1/T_1$ are depressed. In the present results, the local moments begin to develop at 15, 25, 40, and 60 K in fields of 0.30, 1.00, 3.66, and 6.00 T, respectively (see Fig. 4A), whereas $1/T_1$ forms a peak at a much lower temperature when the moments are sufficiently developed. This feature is compatible with our view that the moment generation is not due to spontaneous spin ordering but is induced by the magnetic field. Another extraordinary feature is that the peak value of $1/T_1$ at 0.30 T is as large as ~200 1/s, two orders of magnitude beyond the critically enhanced peak value for the AFM transition of κ-Cu-Cl (*9*, *35*). Furthermore, the $1/T_1$ peak value decreases by orders of magnitude with increasing the magnetic field from 0.30 to 6.00 T, which is not expected for a conventional AFM transition; for example, the reduction in the peak value of $1/T_1$ at the AFM transition in κ-Cu-Cl upon increasing the applied field from 0.58 to 9.3 T was reported to be ~1/5 (*35*). These features of $1/T_1$ show that the peak formation of $1/T_1$ is not due to a magnetic transition, consistent with the results from ac-χ.

Spin correlation time

As seen above, large and extremely field-susceptible fluctuations free from order prevail in the present spin system. A possible way to further study these extraordinary features of $1/T_1$ is the analysis based on the Bloembergen-Purcell-Pound (BPP)–type mechanism, as suggested by Le *et al.* (*30*), which describes $1/T_1$ in terms of the temperature-dependent correlation time of fluctuations, $\tau_c(T)$, as in (*36*, *37*)

$$1/T_1 \sim \gamma^2\overline{h^2}\frac{\tau_c(T)}{1+(2\pi f_o)^2\tau_c(T)^2} \quad (1)$$

with the nuclear gyromagnetic ratio γ, mean square of local field fluctuations, $\overline{h^2}$, and the nuclear Larmor frequency f_o. In general, the values of $\tau_c(T)$ increases upon cooling, and when it reaches the value of $(2\pi f_o)^{-1}$, $1/T_1$ forms a peak with a value of $\gamma^2\overline{h^2}(2\pi f_o)^{-1}/2$ at a temperature T_{peak}. Above T_{peak}, because $\tau_c(T) << (2\pi f_o)^{-1}$, $1/T_1 \sim \gamma^2\overline{h^2}\tau_c(T)$, which is f_o independent, whereas below T_{peak}, because $\tau_c(T) >> (2\pi f_o)^{-1}$, $1/T_1 \sim \gamma^2\overline{h^2}2\pi f_o^{-2}\tau_c(T)$, which is inversely proportional to f_o^2. In the present results, the low-field $1/T_1$ data for 0.30 T (f_o = 12.8 MHz)

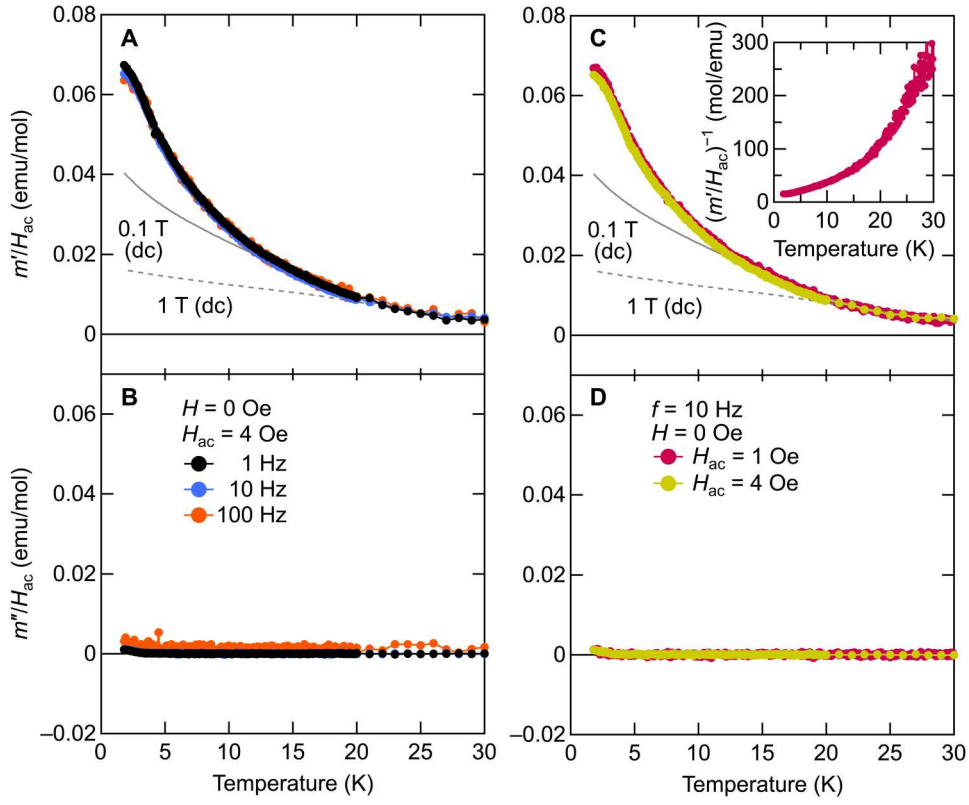

Fig. 5. ac magnetization. Temperature dependence of the real part and imaginary part of ac susceptibility, m'/H_{ac} and m''/H_{ac}. The results plotted in (**A**) and (**B**) were obtained with an ac driving field H_{ac} of 4 Oe in the frequency range of 1 to 100 Hz. The results plotted in (**C**) and (**D**) were obtained with H_{ac} of 1 and 4 Oe at a frequency of 10 Hz. The inverse of m'/H_{ac} obtained with H_{ac} of 1 Oe is plotted in the inset of (C).

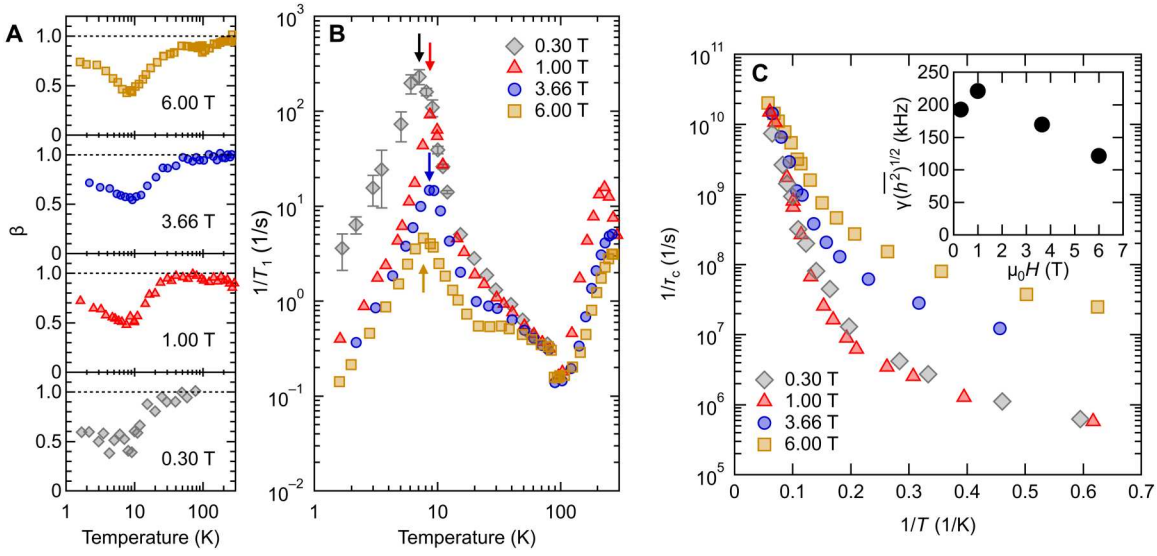

Fig. 6. ^{1}H nuclear spin-lattice relaxation. (**A**) Exponent β obtained from the stretched exponential fit to the nuclear magnetization recovery. The horizontal lines of β = 1 correspond to the homogeneous limit. (**B**) Temperature dependence of the ^{1}H nuclear spin-lattice relaxation rate, $1/T_1$. The arrows indicate the peak temperature, T_{peak}. (**C**) Arrhenius plot of the inverse of correlation time of spin fluctuations, $\tau_c(T)$ below ~20 K, which was derived from the BPP analyses (see the main text) of the $1/T_1$ data shown in (B). (Inset) Field dependence of the amplitude of local field fluctuations, $\gamma\sqrt{\overline{h^2}}$.

and 1.00 T (f_o = 42.4 MHz) nearly coincide above T_{peak} and differ by a factor of 10 [nearly corresponding to $(42.4/12.8)^2$] below T_{peak} (Fig. 6B), which supports the validity of the BPP description. When the magnetic field is increased up to 6 T, $1/T_1$ is depressed in a wide temperature range around T_{peak}, which suggests that $\gamma^2\overline{h^2}$ and/or $\tau_c(T)$ depend on the magnetic field strength. Figure 6C displays $\gamma\sqrt{\overline{h^2}}$ (inset) and $1/\tau_c(T)$ (main panel) derived in the following way: First, $\gamma\sqrt{\overline{h^2}}$ for each magnetic field was evaluated from the peak value through $1/T_1 = \gamma^2\overline{h^2}(2\pi f_o)^{-1}/2$; then, $\tau_c(T)$ was calculated from Eq. 1, using the $\gamma\sqrt{\overline{h^2}}$ value for each field. The $\gamma\sqrt{\overline{h^2}}$ values for the low fields of 0.30 and 1.00 T are ~200 kHz, which roughly correspond to the local field generated by one μ_B on an ET dimer (see the preceding subsection). This means that the moments fluctuate in all directions. $\gamma\sqrt{\overline{h^2}}$ decreases upon increasing the field to 3.66 and 6.00 T, which is ascribable to the gradual restriction of orientational fluctuations of spins around the field direction. These features confirm that the spins are in a paramagnetic state.

The value of $1/\tau_c(T)$ is ~10^{10} to 10^{11} 1/s at high temperatures and rapidly decreases with temperature below ~15 K. The $1/\tau_c(T)$ value is field dependent below ~15 K, where the local moments and magnetization are nonlinearly induced by the magnetic field (see Fig. 4). Upon application of low magnetic fields of 0.30 and 1.00 T, $1/\tau_c(T)$ drops to below the megahertz range at low temperatures. This means that the spectral weight of fluctuations shifts downward below the MHz range upon cooling, consistent with the increase in $1/T_2$ of ^{13}C nuclei (*30*). This explains the apparent freezing of the moment with low fields of 0.30 and 1.00 T at 2 and 3 K (see Fig. 4G); when the moment fluctuations are slower than the NMR observation frequency, NMR sees a snapshot of the local fields even if the paramagnetic moments fluctuate. This is further supported by the additional increase in linewidth, $\langle\Delta f^2\rangle_m^{1/2}$, below ~5 K, where $1/\tau_c(T)$ is well below the NMR observation frequency at 0.30 and 1.00 T (Fig. 4A). Namely, the moments likely remain unfrozen at least down to 2 K, consistent with the magnetization (Fig. 4H) and ac-χ behavior (Fig. 5). At higher fields, 3.66 and 6.00 T, the $1/\tau_c(T)$ values are one or two orders of magnitude larger than those at the lower fields, suggesting that the fluctuations become stiffer in the strong magnetic fields, which forces the moments to orient to the field direction. Intriguingly, $1/\tau_c(T)$ does not show Arrhenius-type behavior but appears to tend toward finite values with no indications of freezing in any magnetic field, preserving the possibility of a quantum liquid phase.

Considering the inhomogeneities of local fields, $1/\tau_c$ should be described with a statistical distribution. Using the expanded exponential correlation function $\langle H_{local}(0)H_{local}(\tau)\rangle \propto \exp.\ [-(|\tau|/\tau_c)^\alpha]$ (*38*, *39*), which is reduced to the BPP formula, Eq. 1, in the case of $\alpha = 1$, a direct fit to the low-temperature $1/T_1$ peak in Fig. 6B with the expression

$$1/T_1 = \int_{-\infty}^{+\infty}\langle H_{local}(0)H_{local}(\tau)\rangle\cos(2\pi f_o\tau)d\tau \qquad (2)$$

yields the activation energy E_a of 40 to 100 K, depending on the magnetic field (see also the Supplementary Materials for further details). Evidently, the obtained E_a is more than an order of magnitude larger than the Zeeman energy in every magnetic field and tends to decrease with increasing field strength. This is totally unexplainable by impurity spins in contrast to the $1/T_1$ behavior in the charge-ordered insulator κ-Hg-Cl, where the peak structure of $1/T_1$ follows the BPP model with E_a equal to the Zeeman energy (*40*). We further discuss the irrelevance of quenched disorder to the behavior of κ-Hg-Br in a later section.

Formation of inhomogeneous spin clusters

Upon cooling from well above 20 K, the inhomogeneous local moments and uniform magnetization that are linearly induced by the magnetic field increase as if they diverge at 20 to 25 K and exhibit Curie-Weiss behavior, $\langle m_{local}\rangle/H = [(1.7 \pm 0.15)\mu_B]^2/3k_B(T - 25)$ per dimer (Fig. 4E) and $M/H = (0.95\ \mu_B)^2/3k_B(T - 20)$ per dimer (Fig. 4F), respectively. Upon further cooling, however, both level off, and a paramagnetic state persists down to well below these temperatures, which indicates that the spin correlation length ceases to grow after reaching a certain finite length at 20 to 25 K. At further lower temperatures, local moments are nonlinearly induced by the magnetic field to afford values as large as ~μ_B; however, the induced magnetization is an order of magnitude smaller. These behaviors require that the local moments should be in a staggered-like configuration and further suggest that the spins form clusters, each of which consists of AFM-configured moments with weak ferromagnetism, but the spin clusters remain paramagnetic and decelerate their fluctuations to the submegahertz range with a number of spins in each cluster swaying together.

The behavior is reminiscent of superparamagnetic behavior. Then, we analyzed the $M(T)$ and $M(H)$ data based on a model (*41*, *42*) widely applied to superparamagnetic systems (*41*–*47*) with parameters of moment per cluster (μ), saturation moment per dimer (M_s), and mean-field Curie-Weiss temperature (T_0). It yields good fits to $M(T)$ with T_0 of 20 to 25 K, which corresponds well to the Weiss temperatures, under every magnetic field (Fig. 4, E and F). The fitted μ and M_s values, however, are strongly field dependent unlike conventional superparamagnetic systems, and the M_s value obtained from the low-field data, ~0.02 μ_B per dimer, is unphysically smaller than the high-field M values, 0.07 to 0.08 μ_B per dimer (Fig. 4H). These results indicate that a description as a conventional superparamagnetic system is inadequate for κ-Hg-Br and very likely originate from the fact that κ-Hg-Br remains paramagnetic even below T_0 at low fields, whereas a conventional superparamagnetic system exhibits a broadened FM transition or spin freezing at around T_0. Using the $M(T)$ data acquired at magnetic fields of 3.66 and 6.00 T, at which spins are highly polarized at low temperatures, yields the values for M_s, ~0.07 μ_B per dimer, and μ, ~4 to 5 μ_B, which correspond to a cluster size of $n = \mu/M_s$ = 50 to 75 spins per cluster. The fits to $M(H)$ also yield temperature-dependent M_s and μ values; however, the fits at low temperatures (2 and 3 K), at which magnetization is traced nearly up to saturation, give consistent values of M_s ~ 0.07 to 0.08 μ_B per dimer and μ ~ 4.5 to 6 μ_B, yielding n = 55 to 85 spins per cluster. Thus, this conventional analysis estimates the cluster size to be 50 to 100 spins. The Curie constant per dimer, $(0.95\ \mu_B)^2$, does not contradict the cluster model; given that the cluster moment μ is carried by n spins, $(0.95\ \mu_B)^2$ is equal to μ^2/n, the effective moment per spin, μ/n, is 0.95 $\mu_B/n^{1/2}$, which yields ~0.095 to 0.13 μ_B per dimer for n = 50 to 100 and corresponds well to the saturated magnetization, 0.07 to 0.08 μ_B per dimer (Fig. 4H), with the factor $[S(S + 1)]^{1/2}/S = 1.73$. Assuming a two-dimensional cluster, the cluster radius, ξ, is estimated through $n = \pi\xi^2$ to be four to six spin sites.

The spectral shape reflects the distribution profile of the field-induced staggered moments. The broadened ^{1}H NMR spectra indicate a continuous distribution of the AFM moment on the molecules in clusters. This is consistent with the nearly continuous distribution of spin density, as signified by the structureless and broadened ^{13}C NMR spectra seen at high temperatures just below T_{MI} (*30*). This spectral feature means that the spin density is imbalanced in a dimer and the imbalanced profile differs from dimer to dimer, resulting in inhomogeneous interactions between spins and thus causing an inhomogeneous AFM configuration of local moments in a cluster. In addition, the ^{1}H NMR spectra with no two-component structure suggest that all spins participate in forming clusters, unlike clusters emerging in a matrix, so that spins coupled with rather stronger interactions define the clusters, which mutually interact through the weakest interactions. To gain further insight into the spin-density distribution, we calculated the spectral widths at 6.00 T, defined by the half-widths at 5, 15, 30, and 50% of the maximum value, $\Delta f_{5\%}$, $\Delta f_{15\%}$, $\Delta f_{30\%}$, and $\Delta f_{50\%}$, respectively. Figure 7A shows the temperature dependence of these spectral widths, each of which exhibits a distinctive temperature dependence. On cooling, the value of $\Delta f_{5\%}$ appreciably increases from 50 K and saturates below 20 K, while this feature is less clear for $\Delta f_{15\%}$ and further so for $\Delta f_{30\%}$, and $\Delta f_{50\%}$ no longer has the convex structure at approximately 20 K but conversely accelerates its increase below 20 K. These features are better characterized by the relative widths of Δf_x (x = 5, 15, and 30%) to $\Delta f_{50\%}$, $\Delta f_x^{rel}(T) \equiv \Delta f_x(T)/\Delta f_{50\%}(T)$, which are plotted in Fig. 7B. This illustrates that the spatial nonuniformity of the local moments progresses upon cooling from 50 K down to 20 K, where the maximum value (represented by $\Delta f_{5\%}$) increases more rapidly than the average value ($\Delta f_{50\%}$), suggesting progressive clustering of spins. In the temperature range of 20 to 50 K, the spin clusters gradually take shape with the development of middle-scale staggered spin configurations.

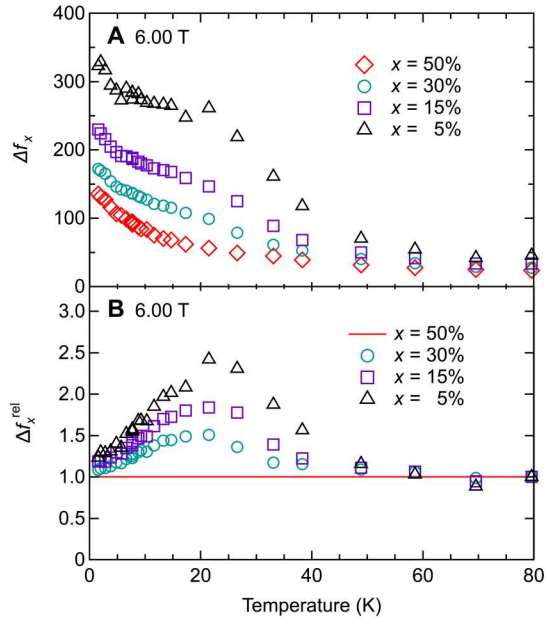

Fig. 7. Temperature dependence of the ^{1}H NMR spectral shape in a field of 6.00 T. (**A**) NMR linewidths determined by the half-widths at 50, 30, 15, and 5% of the maximum value, $\Delta f_{50\%}$, $\Delta f_{30\%}$, $\Delta f_{15\%}$, and $\Delta f_{5\%}$. (**B**) Relative linewidth, Δf_x^{rel} (x = 50, 30, 15, and 5%), normalized at 80 K (see the main text for the definition).

An important feature of the spin clustering in κ-Hg-Br is that the staggered magnetization is induced by a uniform external field, which usually does not cause staggered moments in the conventional paramagnetic state because the uniform field is not conjugated to the staggered magnetization. A conceivable origin is the Dzyaloshinskii-Moriya (DM) interaction, which induces staggered moments under a uniform applied field in the paramagnetic state (*12*) as well as spin canting in the AFM ordered state (*10*–*12*, *14*). However, the DM interaction fails to explain the feature in question because it necessarily gives uniform susceptibility with the Weiss temperature of the opposite sign to that of the staggered susceptibility, as we show with the mean-field calculations of the AFM Heisenberg model with the DM interactions in the Supplementary Materials. Furthermore, the spin canting angle, which measures the DM interaction relative to the exchange interactions, is only 0.3° for κ-Cu-Cl (*10*–*12*) and κ-Cu-Br (*14*) owing to the small spin-orbit interaction; in the present system, however, the canting angle is estimated to be ~3° from the ratio of the staggered and uniform magnetizations at low temperatures, which is apparently too large to be explained by DM interactions. Thus, field-induced staggered and uniform magnetizations with similar Weiss temperatures require a different mechanism that makes AFM and FM correlations grow in parallel, albeit with different magnitudes, or AFM and FM moments mutually locked within each cluster and further causes FM interactions between clusters. Regarding the intercluster interactions, Yamashita *et al.* (*29*) proposed an interesting microscopic mechanism that causes FM interactions between one-dimensional spin fragments. The model assumes a stripy charge order hosting one-dimensional finite-size spin-singlet chains, which are interrupted by defect-like spins whose locations fluctuate between two ET sites within the dimer (called dimer spins). Then, the model predicts that the dimer spins mediate FM coupling between the right- and left-side adjacent charge-ordered spins and induce spatially varied staggered moments in the spin singlet chains. This model appears to explain the key experimental features, such as formation of inhomogeneous staggered moments and FM coupling between clusters. We note, however, that the observed field-induced local moments are as large as the order of μ_B on average, which necessitates very short one-dimensional spin fragments divided by dense dimer spins to be consistent with this model. Such FM centers are expected to give asymmetric NMR spectra with different shapes from the background AFM spectrum if their concentration is at the level of approximately 10% or more. The spectra at low temperatures under high magnetic fields of 3.66 and 6.00 T bear shoulders on the higher frequency side (Fig. 2, C and D), which may indicate the presence of the FM centers. If so, the FM centers should be distributed even within a cluster because each cluster consists of dozens of spins. As revealed by the NMR spectra and relaxation, the local moments are considerably inhomogeneous in magnitude so that the FM coupling, if any, can be significantly distributed in magnitude as well; it is possible that weak couplings give rise to the intercluster FM interactions, whereas stronger couplings are responsible for ferromagnetism in each cluster, which coherently explains the present observation. In (*28*), the emergence of FM polarons is suggested as an origin of FM interaction in the present system. The

above model may involve a novel type of FM polaron that emerges from the AFM background.

Effects of structural disorder and impurity

Structural defects or impurities can have nonnegligible effects on the magnetic properties of frustrated spin systems (*48*), and recently, the effect of defects and impurities on the physical properties of QSL materials has been recognized as an important issue [for examples, see (*49*, *50*) and the references therein]. Regarding NMR, it is known that structural defects and magnetic or nonmagnetic impurities induce staggered responses in frustrated systems, e.g., $SrCr_{9p}Ga_{12-9p}O_{19}$ (*51*), $Cu_3V_2O_7(OH)_2{\cdot}2H_2O$ (*52*), and $ZnCu_3(OH)_6Cl_2$ (*53*, *54*), similar to unfrustrated AFM spin systems (*55*). We discuss the present observations from this perspective.

In general, these effects manifest themselves at low temperatures well below the energy scale of the exchange interaction and, in particular, are remarkable in the spin-singlet ground state. In this case, magnetic signatures are observed upon cooling after the majority of spins fall into the nonmagnetic state. This is well exemplified by the previous ^{1}H NMR study of the sister compound, κ-Hg-Cl;$1/T_1$, which shows a drop suggesting a nonmagnetic transition at 20 K and then exhibits a broad peak at approximately 5 K, was attributed to impurity effects (*40*). The present system, however, shows no indication of a nonmagnetic phase in either the ^{1}H NMR or ^{13}C NMR properties (*30*) and shows an extremely large peak value of ^{1}H $1/T_1$, which is two to three orders of magnitude beyond that observed for κ-Hg-Cl (see the Supplementary Materials). Furthermore, the sizable field-induced staggered moments on average in κ-Hg-Br (see the right axes of Fig. 4A) are not reconciled with the defect(impurity)-induced staggered response of minority spins in a nonmagnetic state. We also note that the Curie-like magnetization upturn suggestive of orphan spins is not observed at the lowest temperatures (Fig. 4B).

Another possibility involves disruption of long-range magnetic order caused by quenched disorder. As described in the preceding sections, our observations strongly rule out spin freezing. Further support for excluding the spin glass state is lent by the spin glass behavior of the x-ray–irradiated κ-Cu-Cl (*56*–*58*). When irradiated by x-rays, the pristine AFM long-range order in κ-Cu-Cl collapses into a line-broadened inhomogeneous spin frozen state (*57*, *58*) and eventually evolves into a QSL-like state without line broadening after further irradiation (*56*). While the structureless broad features of the ^{1}H NMR spectra appear to be common to both κ-Hg-Br and the spin-frozen κ-Cu-Cl, a comparison of the temperature dependences of $1/T_1$ and $\langle \Delta f^2 \rangle^{1/2}$ reveals a significant difference between the two systems. As discussed in the previous section, one of the unique characteristics of κ-Hg-Br is that the spectra are broadened at much higher temperatures than the peak temperature in $1/T_1$, T_{peak}. In the x-ray–irradiated κ-Cu-Cl, however, the spectral broadening begins at nearly the same temperature as T_{peak}, as expected for spin glass systems in general. Thus, a comparison of the two systems highlights the peculiar magnetism of κ-Hg-Br out of the conventional spin glass framework. In addition, there is no difference between the field-cooled and zero-field-cooled magnetic susceptibilities, which rules out the spin glass state (see the Supplementary Materials).

In terms of the crystal structure, several κ-type ET compounds exhibit inevitable disorder of ionic configurations in the insulating anion layer, such as disorder involving CN or NC in κ-Cu-CN (*59*, *60*). However, κ-Hg-Br has no structural randomness in the $Hg(SCN)_2Br$ anion layers (*30*, *61*). Another possible source of structural disorder is glassy freezing of the ethylene conformations in ET (Fig. 1C), which has been observed for several ET salts and proposed as the origin of the inhomogeneity in κ-Hg-Br by Le *et al.* (*30*). This type of disorder can have a critical influence on the electronic state in the vicinity of a phase boundary by modulating the electronic bandwidth and introducing disorder (*62*). According to the low energy effective model of charges (*29*, *63*), the first-principles–based evaluation (*27*) predicts κ-Hg-Br to be situated close to the boundary between the dimer-Mott and charge-ordered states; thus, the ethylene disorder, if any, might have a critical influence on the electronic state. In such cases, a key is the cooling-rate dependence of the physical properties. To the best of our knowledge, there have been no reports indicating glassy freezing of the ethylene groups in κ-Hg-Br. However, for the sister compound, κ-Hg-Cl, the thermal expansion study revealed that the glass transition of the ethylene groups could be controlled by the cooling rate (*64*). We examined the cooling-rate dependence of the magnetic susceptibility of κ-Hg-Br at 0.2 and 0.02 K/min but found no appreciable difference in behavior (see the Supplementary Materials). In addition, we note that clear charge ordering is observed for θ-$(ET)_2RbZn(SCN)_4$ with disordered ethylene groups (*65*). Thus, we suggest that the ethylene disorder is not the primary source of the observed inhomogeneities and curious magnetic behavior of κ-Hg-Br.

DISCUSSION

To elucidate the microscopic spin state in the dipole liquid candidate κ-$(ET)_2Hg(SCN)_2Br$, we conducted ^{1}H NMR studies with magnetic fields varied over a 20-fold range. The field and temperature dependence of the NMR spectrum indicates that staggered moments are inhomogeneously and nonlinearly induced by a magnetic field and reach the order of μ_B per ET dimer in a magnetic field of a few tesla at low temperatures. The temperature dependence of NMR $1/T_1$ exhibits a pronounced peak at ~7 to 9 K ascribable to noncritical slowing down of spin fluctuations instead of the critical enhancement associated with a magnetic transition. The present analyses of the NMR spectra and $1/T_1$ and the fitting of the conventional model to magnetization behavior lead to the following picture for the spin state in κ-$(ET)_2Hg(SCN)_2Br$: The spins with short-ranged AFM and FM correlations develop their moments heterogeneously upon cooling as if both correlations diverge at ~20 to 25 K, shaping inhomogeneous spin clusters. Below ~20 K, however, the spin clusters remain paramagnetic and their dynamics gradually slows down to frequencies below the megahertz range without any indication of spin ordering or freezing down to 1.8 K, as confirmed by ac susceptibility data. Intriguingly, slowing down of the spin fluctuations is not of the activation type and tends to cease at low temperatures with the correlation time saturating to a finite value. These slowly fluctuating spin clusters maintain liquidity even at low temperatures, and this spin clustering can be a novel type of spin organization, free from ordering or freezing, that emerges in a system with both of charge and spin frustrations; in the case of κ-Hg-Br, band filling for the geometrically frustrated triangular lattice is on the verge between quarter- and half-filling (*26*, *27*). The Raman data do not show a clear charge imbalance, which is suggestive of a Mott-insulator with a half-filled nature

(*23*), whereas ^{13}C NMR data indicate charge disproportionation of a quarter-filled nature below T_{MI} (*30*). These apparently contradicting features possibly suggest the dual characteristics of κ-Hg-Br, namely, Mottness and charge-imbalanced instability, and may be attributed to NMR probing the spin degrees of freedom preferentially and Raman scattering probing the charge degrees of freedom in different manners. It is noted that such a discrepancy between the charge-density profiles probed by NMR and Raman scattering was observed for another charge-frustrated system (*66*–*68*). Thus, κ-Hg-Br very likely verges on charge instability, and furthermore, the triangular lattice imposes frustration on the interacting spins, as in other κ-type ET salts.

Last, the present observations of middle-scale clustering instead of long-range order, noncritical slowing down of spin fluctuations, and anomalously field-susceptible magnetic behavior are reminiscent of soft matter such as polymers, colloids, and liquid crystals. They are characterized by constituent elements having many internal degrees of freedom, and their spatiotemporal characteristics are middle-scale (on the order of tens to hundreds of nanometers) correlation instead of ordering, slow fluctuations that decelerate toward lower temperatures, and enhanced responsiveness (deformation) to external forces (*69*). The present system can be a spin version of soft matter and thus provides a way to share a similar concept between quantum magnetism and soft matter physics.

MATERIALS AND METHODS

Sample preparation

The samples of κ-Hg-Br were synthesized by the electrochemical method.

^{1}H NMR measurements

We performed ^{1}H NMR experiments in magnetic fields of 0.30, 1.00, 3.66, and 6.00 T applied nearly parallel to the *a* axis of a single crystal weighing 0.31 mg (#1) and obtained NMR spectra and nuclear spin-lattice relaxation times, T_1, which probe the near-static and dynamical spin susceptibility, respectively. The ^{1}H NMR spectra were acquired by the standard solid echo method using the pulse sequence $t_{\pi/2}$-τ_i-$t_{\pi/2}$ with the π/2 pulse width $t_{\pi/2}$ and interval time τ_i. Throughout the measurements, $t_{\pi/2}$ was within the range of 0.5 to 2.0 μs, and we confirmed that the spectrum at the lowest temperature, where it was most broadened, was nearly reproduced even when the observation frequency was varied within a range extending ±300 kHz from the center of the spectrum, indicating that the rf pulse covered the entire spectrum. The nuclear spin-lattice relaxation time, T_1, was determined by the standard saturation-recovery method.

dc and ac magnetization measurements

We performed dc and ac magnetization measurements within the temperature range of 1.8 to 300 K using Magnetic Property Measurement Systems (MPMS-5S and MPMS-XL, Quantum Design Inc.) and the MPMS AC option. The dc magnetization data shown in Fig. 4 in the text were obtained for an assembly of four single crystals weighing 2.06 mg in total (#2) in a magnetic field applied nearly parallel to the *a* axis. The first-order metal-insulator transition was signaled by a jump in magnetization at the T_{MI} of approximately 90 K. The magnetization was proportional to the magnetic field without a jump in the low-field limit even below T_{MI}, signifying the paramagnetic nature. In all dc magnetization data, the core diamagnetic contribution of -5.15×10^{-4} emu/mol was subtracted. In the ac susceptibility measurements, we measured an assembly of several tens of single crystal pieces weighing 12.56 mg in total (#3) using a cage made of Kapton film. The sample dependences of the ^{1}H NMR characteristics and dc magnetization are discussed in the Supplementary Materials.

Simulation of ^{1}H NMR spectra and estimation of second moments

To confirm the configuration of local moments and estimate their average size, we simulated the ^{1}H NMR spectra for several conceivable cases of collinear spin configurations (see also the Supplementary Materials for the detailed results). Because the proton nuclei in ET have negligibly small Fermi contact interactions, the local fields at the ^{1}H sites are calculated by adding up dipolar fields from electron moments on the constituent atomic sites. We calculated the ^{1}H NMR spectra, which are to be related to $\langle \Delta f^2 \rangle_m$, using the reported crystal structure of the isostructural κ-Hg-Cl at 100 K (*25*) and considering the minimal Hamiltonian describing the interactions between the pair of the ^{1}H nuclear spins with I_{ji} (i = 1, 2) bonded to the carbon j and the electronic spins in the following

$$\mathscr{H}^j = \sum\nolimits_i (-\gamma\hbar\delta H^z_{ji} I^z_{ji}) + \frac{\gamma^2\hbar^2}{{r_j}^3}\left[I^z_{j1}I^z_{j2} - \frac{1}{4}(I^+_{j1}I^-_{j2} + I^-_{j1}I^+_{j2})\right](1 - 3\cos^2\phi_j) \quad (3)$$

where γ and $\hbar$ are the gyromagnetic ratio of ^{1}H nuclei and the reduced Planck constant, respectively. The first term is the hyperfine interaction between each ^{1}H nuclear spin and all electronic moments; because the magnitude of the hyperfine field, $|\boldsymbol{\delta H_{ji}}|$, is much smaller than that of the applied field, the interaction is well approximated by its z component. The second term comes from the dipole interactions between a pair of ^{1}H nuclear spins under consideration. The distance between the ^{1}H nuclei and the angle between the vector connecting the paired ^{1}H nuclei and an applied magnetic field are denoted as r_j and ϕ_j, respectively. In the present case, the hyperfine field, $\boldsymbol{\delta H_{ji}}$, mainly comes from the electronic dipolar fields, $\boldsymbol{H_{dip,ji}}$; thus, we approximated it as the sum of the external field-parallel component of the point-dipolar fields from all off-site atom positions within a sphere of ~100-Å radius

$$\boldsymbol{H}_{\mathbf{dip},ji} = \sum\nolimits_k \sigma_k \left\{ 3\frac{(\boldsymbol{\mu}_k \bullet \boldsymbol{r}_{ji,k})\boldsymbol{r}_{ji,k}}{{r_{ji,k}}^5} - \frac{\boldsymbol{\mu}_k}{{r_{ji,k}}^3} \right\} \quad (4)$$

where $\boldsymbol{r_{ji,k}}$ is the vector from the atomic site (k) to the proton site (ji) and $r_{ji,\,k} = |\boldsymbol{r_{ji,k}}|$. The prefactor σ_k is the Mulliken charge, the population density of the HOMO, at atom k calculated with the extended Hückel method (*31*), and $\boldsymbol{\mu}_k$ is the total moment of the ET molecule to which atom k belongs. In the present simulation, we ignored the isotropic Fermi contact from the on-site electronic moment or transferred hyperfine couplings via the σ bond to the neighboring carbon because it is, in general, negligibly small in the ET compounds due to the small HOMO densities in the ethylene group that reside at the edges of ET molecules. For a radical ET^+, the hyperfine coupling constant at the ^{1}H site is less than 2×10^1 Oe/μ_B (*70*). We also ignored the moment-independent chemical shift. Note that the present simulations do not consider the demagnetization effect because the uniform magnetization is much smaller than

expected from the fully polarized moments and the main contribution to the local fields is from the staggered-like moments. For reference, the demagnetization factors estimated by the spheroidal approximation of the sample dimension, $1 \times 0.4 \times 0.4$ mm^3, are ~0.43 (0.14) for applying the magnetic field along the short (long) axis of the sample; the field direction in the present study is along one of the short axes.

From Eq. 3, we expect a quartet signal from each pair of protons bonded to the same carbon

$$\Delta E_{1\leftrightarrow 2} = D_{j+} - \sqrt{{D_{j-}}^2 + {J_j}^2} - 2J_j \quad (5)$$

$$\Delta E_{3\leftrightarrow 4} = D_{j+} - \sqrt{{D_{j-}}^2 + {J_j}^2} + 2J_j \quad (6)$$

$$\Delta E_{1\leftrightarrow 3} = D_{j+} + \sqrt{{D_{j-}}^2 + {J_j}^2} - 2J_j \quad (7)$$

$$\Delta E_{2\leftrightarrow 4} = D_{j+} + \sqrt{{D_{j-}}^2 + {J_j}^2} + 2J_j \quad (8)$$

with the intensities

$$I_{1\leftrightarrow 2} = 1 + \sin 2\eta \quad (9)$$

$$I_{3\leftrightarrow 4} = 1 - \sin 2\eta \quad (10)$$

$$I_{1\leftrightarrow 3} = 1 - \sin 2\eta \quad (11)$$

$$I_{2\leftrightarrow 4} = 1 + \sin 2\eta \quad (12)$$

where

$$D_{j\pm} = \frac{1}{2}\gamma\hbar(\delta H^z_{j1} \pm \delta H^z_{j2}),\ J_j = \frac{\gamma^2\hbar^2}{4{r_j}^3}(1 - 3\cos^2\theta_j),\ \tan 2\eta_j = \left|\frac{J_j}{D_{j-}}\right|$$

The total spectrum for an ET molecule consists of 16 lines from four inequivalent pairs of protons. We assumed the Gaussian shape $g(f)$ for each of the spectral lines n (n = 1, 2, ..., 16) with the form $I_n g(f - f_{n0})$, where f_{n0} and I_n are the central position and its intensity of line n is determined by Eqs. 5 to 8 and 9 to 12, respectively. We performed these calculations for magnetically inequivalent ET molecules and constructed the numerical spectrum by superposing all of the lines. Given the pattern for the spin configuration, the simulated $\langle \Delta f^2 \rangle_m^{1/2}$, determined by the second moment of the spectrum after subtraction of that for the spectrum with zero local moments, is proportional to the size of the local spin moments, m_{local}; $\langle \Delta f^2 \rangle_m^{1/2} = a m_{\mathrm{local}}$, with the coefficient a depending on the moment configuration.

Supplementary Materials

This PDF file includes:

Supplementary Text
Figs. S1 to S14
Table S1

REFERENCES AND NOTES

1. M. Imada, A. Fujimori, Y. Tokura, Metal-insulator transitions. *Rev. Mod. Phys.* **70**, 1039–1263 (1998).
2. Y. Zhou, K. Kanoda, T.-K. Ng, Quantum spin liquid states. *Rev. Mod. Phys.* **89**, 025003 (2017).
3. L. Savary, L. Balents, Quantum spin liquids: A review. *Rep. Prog. Phys.* **80**, 016502 (2017).
4. C. Broholm, R. J. Cava, S. A. Kivelson, D. G. Nocera, M. R. Norman, T. Senthil, Quantum spin liquids. *Science* **367**, 263 (2020).
5. J. Knolle, R. Moessner, A field guide to spin liquids. *Annu. Rev. Condens. Matter Phys.* **10**, 451–472 (2019).
6. K. Kanoda, R. Kato, Mott physics in organic conductors with triangular lattices. *Annu. Rev. Condens. Matter Phys.* **2**, 167–188 (2011).
7. K. Miyagawa, K. Kanoda, A. Kawamoto, NMR studies on two-dimensional molecular conductors and superconductors: Mott transition in κ-(BEDT-TTF)$_2$X. *Chem. Rev.* **104**, 5635–5654 (2004).
8. H. Kino, H. Fukuyama, Phase diagram of two-dimensional organic conductors: (BEDT-TTF)$_2$X. *J. Phys. Soc. Jpn.* **65**, 2158–2169 (1996).
9. K. Miyagawa, A. Kawamoto, Y. Nakazawa, K. Kanoda, Antiferromagnetic ordering and spin structure in the organic conductor, κ-(BEDT-TTF)$_2$Cu[N(CN)$_2$]Cl. *Phys. Rev. Lett.* **75**, 1174–1177 (1995).
10. D. F. Smith, S. M. De Soto, C. P. Slichter, J. A. Schlueter, A. M. Kini, R. G. Daugherty, Dzialoshinskii-Moriya interaction in the organic superconductor κ−(BEDT−TTF)$_2$Cu[N(CN)$_2$]Cl. *Phys. Rev. B* **68**, 024512 (2003).
11. R. Ishikawa, H. Tsunakawa, K. Oinuma, S. Michimura, H. Taniguchi, K. Satoh, Y. Ishii, H. Okamoto, Zero-field spin structure and spin reorientations in layered organic antiferromagnet, κ-(BEDT-TTF)$_2$Cu[N(CN)$_2$]Cl, with Dzyaloshinskii-Moriya interaction. *J. Phys. Soc. Jpn.* **87**, 064701 (2018).
12. F. Kagawa, Y. Kurosaki, K. Miyagawa, K. Kanoda, Field-induced staggered magnetic moment in the quasi-two-dimensional organic Mott insulatorκ−(BEDT-TTF)$_2$Cu[N(CN)$_2$]Cl. *Phys. Rev. B* **78**, 184402 (2008).
13. K. Miyagawa, A. Kawamoto, K. Uchida, K. Kanoda, Commensurate magnetic structure in κ-(BEDT-TTF)$_2$X. *Phys. B* **284-288**, 1589–1590 (2000).
14. K. Oinuma, N. Okano, H. Tsunakawa, S. Michimura, T. Kobayashi, H. Taniguchi, K. Satoh, J. Angel, I. Watanabe, Y. Ishii, H. Okamoto, T. Itou, Spin structure at zero magnetic field and field-induced spin reorientation transitions in a layered organic canted antiferromagnet bordering a superconducting phase. *Phys. Rev. B* **102**, 035102 (2020).
15. Y. Shimizu, K. Miyagawa, K. Kanoda, M. Maesato, G. Saito, Spin liquid state in an organic mott insulator with a triangular lattice. *Phys. Rev. Lett.* **91**, 107001 (2003).
16. Y. Shimizu, T. Hiramatsu, M. Maesato, A. Otsuka, H. Yamochi, A. Ono, M. Itoh, M. Yoshida, M. Takigawa, Y. Yoshida, G. Saito, Pressure-tuned exchange coupling of a quantum spin liquid in the molecular triangular lattice κ–(ET)$_2$Ag$_2$(CN)$_3$. *Phys. Rev. Lett.* **117**, 107203 (2016).
17. C. Hotta, Quantum electric dipoles in spin-liquid dimer Mott insulator κ-ET$_2$Cu$_2$(CN)$_3$. *Phys. Rev. B* **82**, 241104(R) (2010).
18. M. Naka, S. Ishihara, Quantum melting of magnetic order in an organic dimer Mott-insulating system. *Phys. Rev. B* **93**, 195114 (2016).
19. M. Abdel-Jawad, I. Terasaki, T. Sasaki, N. Yoneyama, N. Kobayashi, Y. Uesu, C. Hotta, Anomalous dielectric response in the dimer Mott insulator κ–(BEDT-TTF)$_2$Cu$_2$(CN)$_3$. *Phys. Rev. B* **82**, 125119 (2010).
20. K. Yakushi, K. Yamamoto, T. Yamamoto, Y. Saito, A. Kawamoto, Raman spectroscopy study of charge fluctuation in the spin-liquid candidate κ-(BEDT-TTF)$_2$Cu$_2$(CN)$_3$. *J. Phys. Soc. Jpn.* **84**, 084711 (2015).
21. K. Itoh, H. Itoh, M. Naka, S. Saito, I. Hosako, N. Yoneyama, S. Ishihara, T. Sasaki, S. Iwai, Collective excitation of an electric dipole on a molecular dimer in an organic dimer-mott insulator. *Phys. Rev. Lett.* **110**, 106401 (2013).
22. T. Kobayashi, Q.-P. Ding, H. Taniguchi, K. Satoh, A. Kawamoto, Y. Furukawa, Charge disproportionation in the spin-liquid candidate κ−(ET)$_2$Cu$_2$(CN)$_3$ at 6 K revealed by ^{63}Cu NQR measurements. *Phys. Rev. Res.* **2**, 042023(R) (2020).
23. N. Hassan, S. Cunningham, M. Mourigal, E. I. Zhilyaeva, S. A. Torunova, R. N. Lyubovskaya, J. A. Schlueter, N. Drichko, Evidence for a quantum dipole liquid state in an organic quasi-two-dimensional material. *Science* **360**, 1101–1104 (2018).
24. T. Ivek, R. Beyer, S. Badalov, M. Čulo, S. Tomić, J. A. Schlueter, E. I. Zhilyaeva, R. N. Lyubovskaya, M. Dressel, Metal-insulator transition in the dimerized organic conductor κ−(BEDT-TTF)$_2$Hg(SCN)$_2$Br. *Phys. Rev. B* **96**, 085116 (2017).
25. N. Drichko, R. Beyer, E. Rose, M. Dressel, J. A. Schlueter, S. A. Turunova, E. I. Zhilyaeva, R. N. Lyubovskaya, Metallic state and charge-order metal-insulator transition in the quasi-two-dimensional conductor κ-(BEDT-TTF)$_2$Hg(SCN)$_2$Cl. *Phys. Rev. B* **89**, 075133 (2014).
26. E. Gati, J. K. H. Fischer, P. Lunkenheimer, D. Zielke, S. Köhler, F. Kolb, H.-A. K. von Nidda, S. M. Winter, H. Schubert, J. A. Schlueter, H. O. Jeschke, R. Valentí, M. Lang, Evidence for

electronically driven ferroelectricity in a strongly correlated dimerized BEDT-TTF molecular conductor. *Phys. Rev. Lett.* **120**, 247601 (2018).
27. A. C. Jacko, E. P. Kenny, B. J. Powell, Interplay of dipoles and spins in κ−(BEDT−TTF)$_2$X, where X = Hg(SCN)$_2$Cl, Hg(SCN)$_2$Br, Cu[N(CN)$_2$]Cl, Cu[N(CN)$_2$]Br, and Ag$_2$(CN)$_3$. *Phys. Rev. B* **101**, 125110 (2020).
28. M. Hemmida, H.-A. K. von Nidda, B. Miksch, L. L. Samoilenko, A. Pustogow, S. Widmann, A. Henderson, T. Siegrist, J. A. Schlueter, A. Loidl, M. Dressel, Weak ferromagnetism and glassy state in κ−(BEDT−TTF)$_2$Hg(SCN)$_2$Br. *Phys. Rev. B* **98**, 241202(R) (2018).
29. M. Yamashita, S. Sugiura, A. Ueda, S. Dekura, T. Terashima, S. Uji, Y. Sunairi, H. Mori, E. I. Zhilyaeva, S. A. Torunova, R. N. Lyubovskaya, N. Drichko, C. Hotta, Ferromagnetism out of charge fluctuation of strongly correlated electrons in κ-(BEDT-TTF)$_2$Hg(SCN)$_2$Br. *npj Quantum Mater.* **6**, 87 (2021).
30. T. Le, A. Pustogow, J. Wang, A. Henderson, T. Siegrist, J. A. Schlueter, S. E. Brown, Disorder and slowing magnetic dynamics in κ−(BEDT−TTF)$_2$Hg(SCN)$_2$Br. *Phys. Rev. B* **102**, 184417 (2020).
31. T. Mori, A. Kobayashi, Y. Sasaki, H. Kobayashi, G. Saito, H. Inokuchi, The intermolecular interaction of tetrathiafulvalene and bis(ethylenedithio)tetrathiafulvalene in organic metals. Calculation of orbital overlaps and models of energy-band structures. *Bull. Chem. Soc. Jpn.* **57**, 627–633 (1984).
32. Y. Maniwa, T. Takahashi, G. Saito, ^{1}H NMR in organic superconductor β-(BEDT-TTF)$_2$I$_3$. *J. Phys. Soc. Jpn.* **55**, 47–50 (1986).
33. T. Takahashi, T. Tokiwa, K. Kanoda, H. Urayama, H. Yamochi, G. Saito, NMR relaxation in the organic superconductor (BEDT-TTF)$_2$Cu(NCS)$_2$. *Synth. Met.* **27**, A319–A324 (1988).
34. M. Sawada, S. Fukuoka, A. Kawamoto, Coupling of molecular motion and electronic state in the organic molecular dimer Mott insulator β′-(BEDT-TTF)$_2$ICl$_2$. *Phys. Rev. B* **97**, 045136 (2018).
35. I. J. Hamad, A. E. Trumper, P. Wzietek, S. Lefbvre, L. O. Manuel, $1/T_1$ nuclear relaxation time of κ-(BEDT-TTF)$_2$Cu[N(CN)$_2$]Cl: Effect of magnetic frustration. *J. Phys. Condens. Matter* **27**, 8091 (2005).
36. C. P. Slichter, *Principles of Magnetic Resonance* (Springer-Verlag, 1990).
37. N. Bloembergen, E. M. Purcell, R. V. Pound, Relaxation effects in nuclear magnetic resonance absorption. *Phys. Rev.* **73**, 679 (1947).
38. G. Williams, D. C. Watts, Non-symmetrical dielectric relaxation behaviour arising from a simple empirical decay function. *Trans. Faraday Soc.* **66**, 80 (1970).
39. R. Chiba, K. Hiraki, T. Takahashi, H. M. Yamamoto, T. Nakamura, Extremely slow charge fluctuations in the metallic state of the two-dimensional molecular conductor θ−(BEDT−TTF)$_2$RbZn(SCN)$_4$. *Phys. Rev. Lett.* **93**, 216405 (2004).
40. A. Pustogow, T. Le, H.-H. Wang, Y. Luo, E. Gati, H. Schubert, M. Lang, S. E. Brown, Impurity moments conceal low-energy relaxation of quantum spin liquids. *Phys. Rev. B* **101**, 140401(R) (2020).
41. J. I. Gittleman, Y. Goldstein, S. Bozowski, Magnetic properties of granular nickel films. *Phys. Rev. B* **5**, 3609–3621 (1972).
42. J. Z. Sun, L. Krusin-Elbaum, A. Gupta, G. Xiao, S. S. Parkin, Does magnetization in thin-film manganates suggest the existence of magnetic clusters? *Appl. Phys. Lett.* **69**, 1002–1004 (1996).
43. C. P. Bean, J. D. Livingston, Superparamagnetism. *J. Appl. Phys.* **30**, S120–S129 (1959).
44. S. Bedanta, W. Kleemann, Supermagnetism. *J. Phys. D Appl. Phys.* **42**, 013001 (2009).
45. J.-Q. Wang, G. Xiao, Transition-metal granular solids: Microstructure, magnetic properties, and giant magnetoresistance. *Phys. Rev. B* **49**, 3982–3996 (1994).
46. S. A. Makhlouf, F. T. Parker, A. E. Berkowitz, Magnetic hysteresis anomalies in ferritin. *Phys. Rev. B* **55**, R14717(R) (1997).
47. M. S. Seehra, V. S. Babu, A. Manivannan, Neutron scattering and magnetic studies of ferrihydrite nanoparticles. *Phys. Rev. B* **61**, 3513–3518 (2000).
48. A. P. Ramirez, Strongly geometrically frustrated magnets. *Ann. Rev. Mater. Sci.* **24**, 453–480 (1994).
49. J. R. Chamorro, T. M. McQueen, T. T. Tran, Chemistry of quantum spin liquids. *Chem. Rev.* **121**, 2898–2934 (2021).
50. C. Lacroix, P. Mendels, F. Mila, *Introduction to Frustrated Magnetism* (Springer-Verlag, 2011).
51. L. Limot, P. Mendels, G. Collin, C. Mondelli, B. Ouladdiaf, H. Mutha, N. Blanchard, M. Mekata, Susceptibility and dilution effects of the Kagomé bilayer geometrically frustrated network: A Ga NMR study of SrCr$_{9p}$Ga$_{12-9p}$O$_{19}$. *Phys. Rev. B* **65**, 144447 (2002).
52. Z. Hiroi, M. Hanwa, N. Kobayashi, M. Nohara, H. Takagi, Y. Kato, M. Takigawa, Spin-1/2 Kagomé-Like lattice in Volborthite Cu$_3$V$_2$O$_7$(OH)$_2$·2H$_2$O. *J. Phys. Soc. Jpn.* **70**, 3377–3384 (2001).
53. A. Olariu, P. Mendels, F. Bert, F. Duc, J. C. Trombe, M. A. de Vries, A. Harrison, ^{17}O NMR study of the intrinsic magnetic susceptibility and spin dynamics of the quantum Kagome antiferromagnet ZnCu$_3$(OH)$_6$Cl$_2$. *Phys. Rev. Lett.* **108**, 087202 (2008).
54. M. Fu, T. Imai, T.-H. Han, Y. S. Lee, Evidence for a gapped spin-liquid ground state in a kagome Heisenberg antiferromagnet. *Science* **350**, 655–658 (2015).
55. H. Alloul, J. Bobroff, M. Gabay, P. J. Hirschfeld, Defects in correlated metals and superconductors. *Rev. Mod. Phys.* **81**, 45–108 (2009).
56. T. Furukawa, K. Miyagawa, T. Itou, M. Ito, H. Taniguchi, M. Saito, S. Iguchi, T. Sasaki, K. Kanoda, Quantum spin liquid emerging from antiferromagnetic order by introducing disorder. *Phys. Rev. Lett.* **115**, 077001 (2015).
57. M. Urai, K. Miyagawa, T. Sasaki, H. Taniguchi, K. Kanoda, Quantum disordering of an antiferromagnetic order by quenched randomness in an organic Mott insulator. *Phys. Rev. Lett.* **124**, 117204 (2020).
58. R. Yamamoto, T. Furukawa, K. Miyagawa, T. Sasaki, K. Kanoda, T. Itou, Emergence of unconventional spin glass-like state in κ-(ET)$_2$Cu[N(CN)$_2$]Cl by introducing weak randomness. *Phys. Rev. B* **104**, 155107 (2021).
59. U. Geiser, H. H. Wang, K. D. Carlson, J. M. Williams, H. A. Charlier Jr., J. E. Heindl, G. A. Yaconi, B. J. Love, M. W. Lathrop, J. E. Schirber, D. L. Overmyer, J. Ren, M.-H. Whangbo, Superconductivity at 2.8 K and 1.5 kbar in .kappa.-(BEDT-TTF)2Cu2(CN)3: The first organic superconductor containing a polymeric copper cyanide anion. *Inorg. Chem.* **30**, 2586–2588 (1991).
60. T. Hiramatsu, Y. Yoshida, G. Saito, A. Otsuka, H. Yamochi, M. Maesato, Y. Shimizu, H. Ito, H. Kishida, Quantum spin liquid: Design of a quantum spin liquid next to a superconducting state based on a dimer-type ET Mott insulator. *J. Mater. Chem. C* **3**, 1378–1388 (2015).
61. S. V. Konovalikhin, G. V. Shilov, O. A. D'yachenko, M. Z. Aldoshina, R. N. Lyubovskaya, R. B. Lyubovskii, Crystal structures of the organic metals (ET)2[Hg(SCN)Cl2] and (ET)$_2$-[Hg(SCN)$_2$Br]. *Bull. Russ. Acad. Sci. Div. Chem. Sci.* **41**, 1819–1826 (1992).
62. D. Guterding, R. Valentí, H. O. Jeschke, Influence of molecular conformations on the electronic structure of organic charge transfer salts. *Phys. Rev. B* **92**, 081109(R) (2015).
63. C. Hotta, theories on frustrated electrons in two-dimensional organic solids. *Crystals* **2**, 1155 (2015).
64. E. Gati, S. M. Winter, J. A. Schlueter, H. Schubert, J. Müller, M. Lang, Insights from experiment and ab initio calculations into the glasslike transition in the molecular conductor κ−(BEDT−TTF)$_2$Hg(SCN)$_2$Cl. *Phys. Rev. B* **97**, 075115 (2018).
65. P. Alemany, J.-P. Pouget, E. Canadell, Structural and electronic control of the metal to insulator transition and local orderings in the θ-(BEDT-TTF)$_2$X organic conductors. *J. Phys. Condens. Matter* **27**, 465702 (2015).
66. R. Chiba, K. Hiraki, T. Takahashi, H. M. Yamamoto, T. Nakamura, Charge disproportionation and dynamics in θ−(BEDT−TTF)$_2$CsZn(SCN)$_4$. *Phys. Rev. B* **77**, 115113 (2008).
67. K. Yakushi, Infrared and Raman studies of charge ordering in organic conductors, BEDT-TTF salts with quarter-filled bands. *Crystals* **2**, 1291–1346 (2012).
68. H. Murase, S. Arai, T. Sato, K. Miyagawa, H. Mori, T. Hasegawa, K. Kanoda, Observation of classical to quantum crossover in electron glass. arXiv:2205.10795 [cond-mat.str-el] (22 May 2022).
69. R. A. L. Jones, *Soft Condensed Matter* (Oxford Univ. Press, 2002), vol. 23, p. 652.
70. L. Cavara, F. Gerson, D. O. Cowan, K. Lerstrup, An ESR Study of the radical cations of tetrathiafulvalene (TTF) and electron donors containing the TTF moiety. *Helv. Chim. Acta* **69**, 141–151 (1986).
71. K. Momma, F. Izumi, VESTA 3 for three-dimensional visualization of crystal, volumetric and morphology data. *J. Appl. Cryst.* **44**, 1272–1276 (2011).

Acknowledgments: We thank C. Hotta, M. Yamashita, S. Uji, S. Sugiura, and S. Dekura for fruitful discussions. A part of the experiments was performed using facilities of the Cryogenic Research Center and the Institute for Solid State Physics, University of Tokyo. N.D. is grateful for the support of the Visiting Researcher's Program of the Institute for Solid State Physics, University of Tokyo. **Funding:** This work was supported by Japan Society for the Promotion of Science Grant-in-Aid for Scientific Research grant numbers JP18H05225, JP20K20894, JP20KK0060, and JP21K18144; NSF Award DMR-2004074 (N.D.); and The Ministry of Science and Higher Education of the Russian Federation number AAAA-A19-119092390079-8 (E.I.Z., S.A.T., and R.N.L.). **Author contributions:** K.K. and N.D. conceived the project. E.I.Z., S.A.T., and R.N.L. prepared the single crystals. M.U. and K.M. performed the ^{1}H NMR and magnetization measurements. M.U. and Y.W. analyzed the data. All the authors discussed the results. **Competing interests:** The authors declare that they have no competing interests. **Data and materials availability:** All data needed to evaluate the conclusions in the paper are present in the paper and/or the Supplementary Materials.

Submitted 25 November 2021
Accepted 18 November 2022
Published 21 December 2022
10.1126/sciadv.abn1680